Preparation of One-Dimensional CoFe2O4 Nanostructures and Their Magnetic Properties

7 AUTHORS, INCLUDING:

Xiaojuan Liu
Chinese Academy of Sciences
72 PUBLICATIONS 921 CITATIONS

SEE PROFILE

Minfeng Lu
University of Lille Nord de France
42 PUBLICATIONS 380 CITATIONS

SEE PROFILE

Jian Meng
Chinese Academy of Sciences
275 PUBLICATIONS 3,632 CITATIONS

SEE PROFILE

Preparation of Ferrite MFe_2O_4 (M = Co, Ni) Ribbons with Nanoporous Structure and Their Magnetic Properties

Zhongli Wang, Xiaojuan Liu, Minfeng Lv, Ping Chai, Yao Liu, and Jian Meng*

State Key laboratory of Rare Earth Resources Application, Changchun Institute of Applied Chemistry, Chinese Academy of Sciences, Changchun, 130022, P. R. China, and Graduate University of Chinese Academy of Sciences, Beijing, 100049, P. R. China

Spinel ferrite, MFe_2O_4 (M = Co, Ni), ribbons with nanoporous structure were prepared by electrospinning combined with sol−gel technology. The ribbons were formed through the agglomeration of magnetic nanoparticles with PVP as the structure directing template. The length of the polycrystalline ribbons can reach millimeters, and the width of the ribbons can be tuned from several micrometers to several hundred nanometers by changing the concentration of precursor. The nanoporous structure was formed during the decomposition of PVP and inorganic salts. The ribbons exhibited weak saturation magnetizations and low coercivities at room temperature, but at low temperature, saturation magnetizations and coercivities increased a lot, especially for $CoFe_2O_4$ ribbons, reaching 72 emu/g and 1.45 T at 2 k, respectively. These novel magnetic ribbons can potentially be used in micro/nano electronic devices, gas-sensors, and catalysts.

1. Introduction

As a group of magnetic materials, ferrites can be used as recording materials, microwave devices, humidity sensors, and pigments, etc. Spinel ferrites, MFe_2O_4 (M = Co, Ni), are among the most important magnetic materials and have been widely used for electronic applications over the past half century.[1,2] For example, cobalt ferrite has attracted considerable attention because of its large magnetocrystalline anisotropy, high coercivity, moderate saturation magnetization, large magnetostrictive coefficient, chemical stability, and mechanical hardness, which are necessary for magnetic recording devices, magneto-optical recording and electronic devices. However, nickel ferrite is a soft ferrite with lower magnetic coercivity but high electrical resistivity, which makes it an excellent core material for power transformers in electronic and telecommunication applications.

Many attempts have been made to design and synthesize various MFe_2O_4 (M = Co, Ni) nanostructures in order to explore their properties and potential applications.[3] Zero-dimensional ferrite nanoparticles can be synthesized from the decomposition of mixed metal-oleate complexes,[4] alkalide reduction,[5] reverse micelles,[6] and coprecipitation.[7] One-dimensional nanowires and nanotubes have also been synthesized with the presence of templates such as anodic aluminum oxide (AAO),[8] carbon nanotubes,[9,10] and DNA.[11] Two-dimensional films have been prepared by assembling nanoparticles at the air/water interface or on silicon.[12,13] However, little work has been done on other unique morphologies of ferrites in micrometer sizes. Furthermore, it is necessary to develop a new route for the synthesis of novel magnetic microstructures and to investigate their properties.

Electrospinning is a simple and effective method for fabricating ultrathin nanofibers.[14−18] In a typical procedure, a high voltage is applied to a droplet of polymer solution that rests on a sharp conduction tip. With a sufficiently high

TABLE 1: Detailed Experimental Parameters and Corresponding Results of $NiFe_2O_4$

sample	$Ni(Ac)_2 \cdot 4H_2O$ (g)	$Fe(NO_3)_3 \cdot 9H_2O$ (g)	PVP (g)	concentration[a] (%)	width[b] (μm)
1	0.6191	2.000	5	45.8	4−4.5
2	0.5263	1.700	4.3	42.0	2−2.5
3	0.3715	1.200	3.5	36.1	0.6−1

[a] Total concentration of PVP and inorganic salts. [b] Width of ribbons. All samples use the same mixed solvent (5 mL of H_2O and 5 mL of C_2H_5OH).

electrical field, the electrostatic forces can overcome the surface tension of the polymer solution and thus cause the ejection of a thin jet from the tip. The charged jet then undergoes a stretching and whipping process that results in the formation of continuous fibers.[14,15] Initially, this technique was utilized for electrospinning of polymers. Recently, such a technique was extended to the synthesis of nanofibers containing inorganic constituents such as ZnO, TiO_2, SnO_2, WO_3, and $NiFe_2O_4$ oxide nanofibers.[16−20] Through modifying the electrospinning condtions, e.g., increasing the concentration of the sol−gel precursor and feeding rate under a low-humidity environment, Li and co-workers reported the formation of flat ribbons of mesoporous $SrTiO_3$.[21] Submicron-thick silica ribbons could be also prepared using similar methodology.[22] In this article, we demonstrate that electrospinning and simple sol−gel processing can be combined to realize controllable synthesis of ribbon-like ferrites by applying cheap raw materials. The width of the ribbons can be tuned by changing the concentration of the precursor.

2. Experimental Procedures

2.1. Preparation. For preparing the electrospinning solution, 2.0 g $Fe(NO_3)_3 \cdot 9H_2O$ and 0.61 g $Co(CH_3COO)_2 \cdot 4H_2O$ (or 0.62 g $Ni(CH_3COO)_2 \cdot 4H_2O$) were dissolved into a mixed solvent containing 5.0 mL H_2O and 5.0 mL absolute ethanol under magnetic stirring. To this solution, 5.0 g of poly(vinyl

* Corresponding author. Phone: +86-431 85262030. Fax: +86-431-5689041. E-mail: jmeng@ciac.jl.cn.
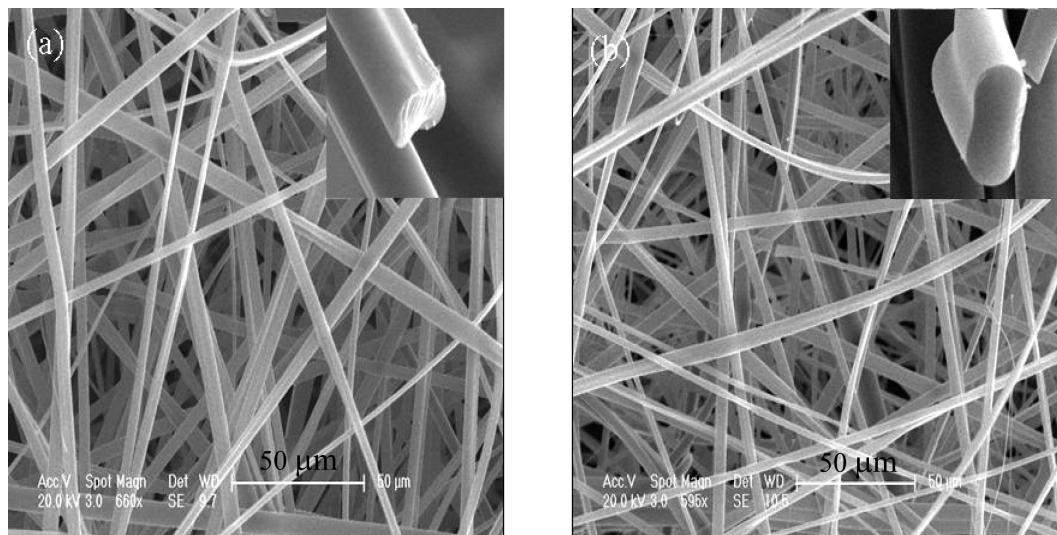
Preparation of Ferrite MFe$_2$O$_4$ Ribbons

J. Phys. Chem. B, Vol. 112, No. 36, 2008 **11293**

Figure 1. SEM images of precursor ribbons: (a)PVP/Fe(NO)$_3$,Co(Ac)$_2$ and (b) PVP/Fe(NO)$_3$,Ni(Ac)$_2$.
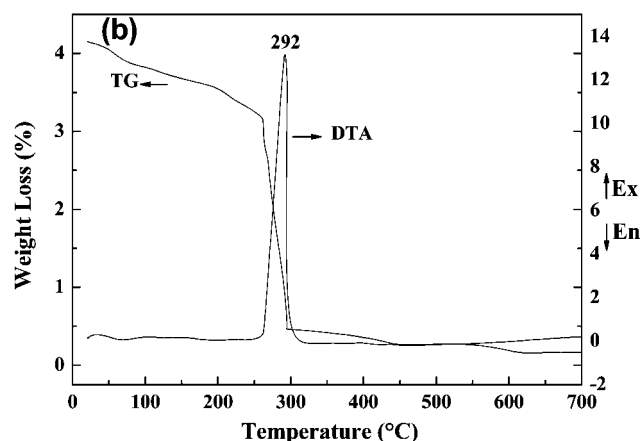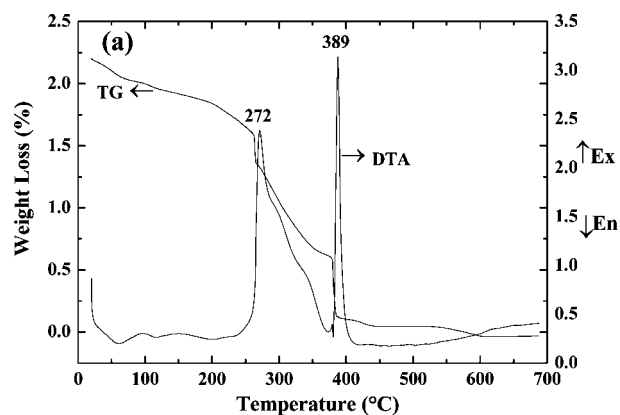
Figure 2. TG-DTA curves of the as-spun ribbons (a) PVP/Fe(NO)$_3$,Co(Ac)$_2$ and (b) PVP/ Fe(NO)$_3$,Ni(Ac)$_2$.

Figure 3. XRD patterns for (a) CoFe$_2$O$_4$ ribbons and (b) NiFe$_2$O$_4$ ribbons.

pyrrolidone) (PVP, K $-$30, Mw $=$ 50,000) was added, and a transparent solution was formed after 12 h stirring.

The as-prepared solution was viscous and was transferred into a hypodermic syringe. The positive terminal of a variable high voltage power supply was connected to the needle tip of the syringe, while the other was connected to the mirror-looking collector plate. The applied voltage was 30 kV, and the distance between the needle tip and the collector was set as 15 cm.[23] After the completion of spinning, the as-prepared samples were first dried at 80 °C for 12 h, then calcined in air at 550 °C for
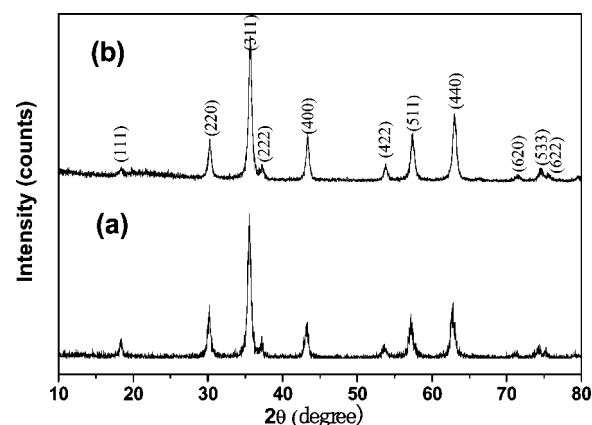
2 h. The heating rate was set at 2 °C /min during the elevation process from room temperature to 550 °C.

To investigate the relationship between width of ribbons and the concentration of the precursor, a series of mixed solutions containing various concentrations of Fe(NO$_3$)$_3$·9H$_2$O, Ni(CH$_3$COO)$_2$·4H$_2$O and PVP were prepared, and subsequent electrospinning and calcination processes were carried out. Detailed experimental parameters and corresponding results for these processes are summarized in Table 1.

2.2. Characterization. Thermogravimetric (TG) and differential thermal analysis (DTA) were carried out on a TA SDT 2960 simultaneous thermal analyzer in air with a heating rate of 10 °C/min. X-ray diffraction (XRD) patterns were collected on a Rigaku-D/max 2500 V X-ray diffractometer equipped with Cu Kα radiation ($\lambda = 1.54178$ Å) at a step width of 0.02°/S. The morphologies and structures of the as-synthesized ferrite products were observed under field emission scanning electron microscopy (FE-SEM) and transmission electron microscopy (TEM). N$_2$ adsorption−desorption isotherms were measured at 77 K using an ASAP 2010 instrument. Specific surface areas were calculated using the Brunauer−Emmett−Teller (BET) model, and the pore size distributions were evaluated from the desorption branches of the nitrogen isotherms using the Barrett−Joyner−Halenda (BJH) model. The magnetic properties of the samples were investigated by a superconducting quantum interference device (SQUID) magnetometer at 300 and 2 K.
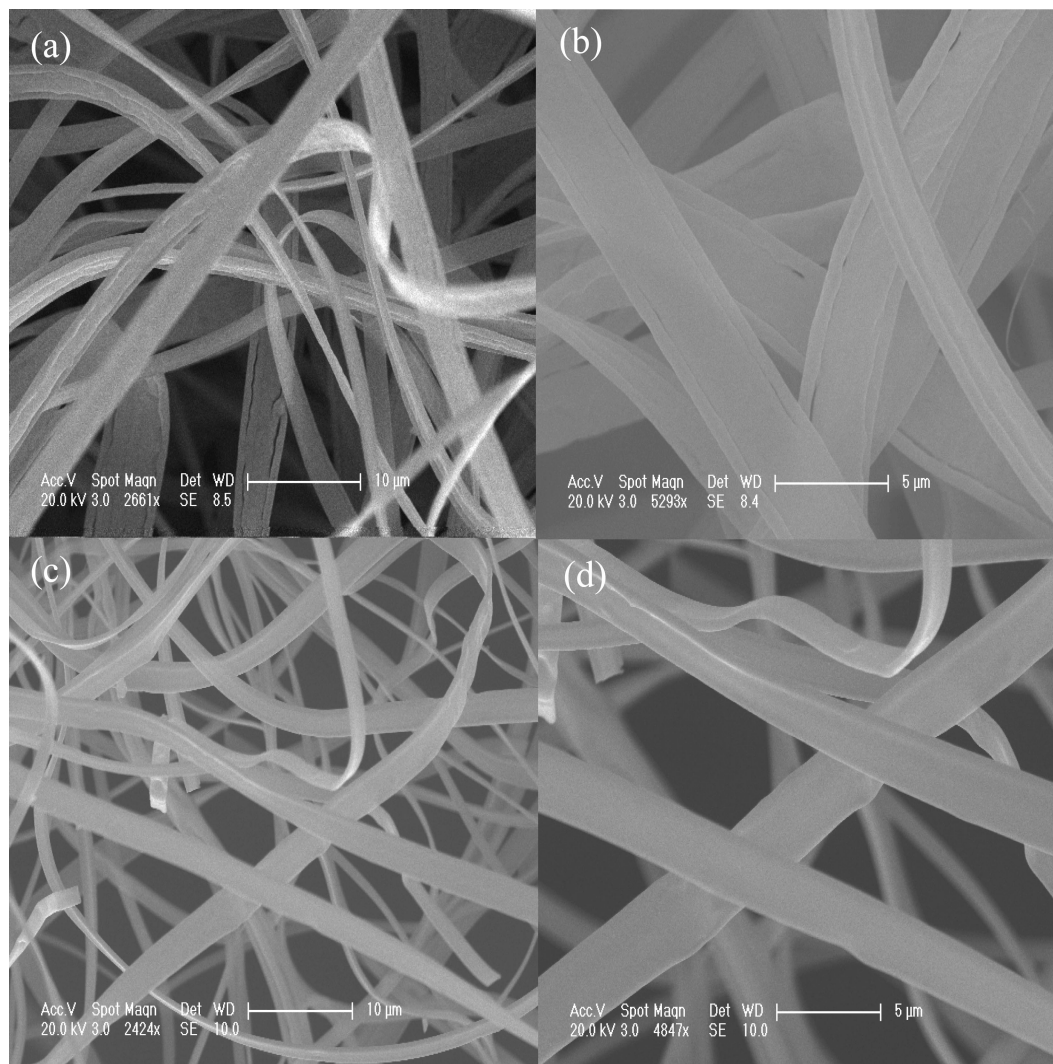
Figure 4. SEM images of the ferrite ribbons calcined at 550 °C in air: (a) and (b) $CoFe_2O_4$ ribbons; (c) and (d) $NiFe_2O_4$ ribbons.

3. Results and Discussion

3.1. Morphological Characteristics and Thermal Properties of the Precursor Ribbons. During the electrospinning process, the evaporation of the solvents in the solution containing all PVP and inorganic salts lead to the formation of gel-like amorphous precursors. As can be seen from SEM results (Figure 1), the amorphous precursors show one-dimensional structure with length up to millimeters. Since a compressed cross section with width around 5.0 μm and thickness about 2.0 μm could be clearly observed in the inset of Figure 1a and b, it can be viewed as a ribbon-like one-dimensional structure. The collected ribbons show random orientation because of the bending instability associated with the spinning jet.

The results of TGA-DTA of the as-spun composite ribbons are shown in Figure 2. Most of the organic material (PVP), NO_3^-, and CH_3COO^- groups and the other volatiles (H_2O, ethanol, etc.) were removed below 450 °C in two samples. The two exothermic peaks at 272 °C in Figure 2a and at 292 °C in Figure 2b in the DTA curves correspond to the decomposition of inorganic salts and the degradation of PVP, which has two degradation mechanisms involving both intra and intermolecular transfer reactions.[24] The exothermic peak at 389 °C in Figure 2a is the result of the oxidation of carbon and carbon monoxide released by the PVP decomposition. There is an obvious difference between the two samples. One possible reason is that

$CoFe_2O_4$ has high magnetocrystalline anisotropy energy, and $CoFe_2O_4$ nanoparticles behave as strongly interacting systems,[25] which lead to the aggregation of nanoparticles especially in submicron thick ribbons. A small part of carbon was enwrapped and needed a high temperature to oxide. Therefore, the surface of the $CoFe_2O_4$ ribbons is not flat, which can be seen in the following TEM images. Interestingly for the PVP/Fe$(NO)_3$, Co$(Ac)_2$ precursor ribbons, when the ribbons become nanometer grade, the TG-DTA curve becomes similar to that of PVP/Fe$(NO)_3$, Ni$(Ac)_2$.

3.2. Structure Analysis, Morphological Characteristics, and Porosity Properties. The XRD patterns of composite ribbons calcined at 550 °C are shown in Figure 3. The diffraction peaks and relative intensities of both patterns match well with JCPDS 03-0864 for $CoFe_2O_4$ ribbons (Figure 3a) and JCPDS 10-0325 for $NiFe_2O_4$ ribbons (Figure 3b), respectively. The formed $CoFe_2O_4$ and $NiFe_2O_4$ ribbons are both cubic spinel structure (space group: Fd-3m (227)). The calculated lattice parameter is 8.366 Å for $CoFe_2O_4$ and 8.342 Å for $NiFe_2O_4$. No impurity phase was found in both patterns.

Figure 4 shows the SEM micrographs of the $CoFe_2O_4$ and $NiFe_2O_4$ ribbons calcined at 550 °C. A well-defined ribbon texture is still maintained, which indicates that PVP acts as the structure directing template during the whole synthesis process. The average width of the ribbons decreased to 4 μm, and average
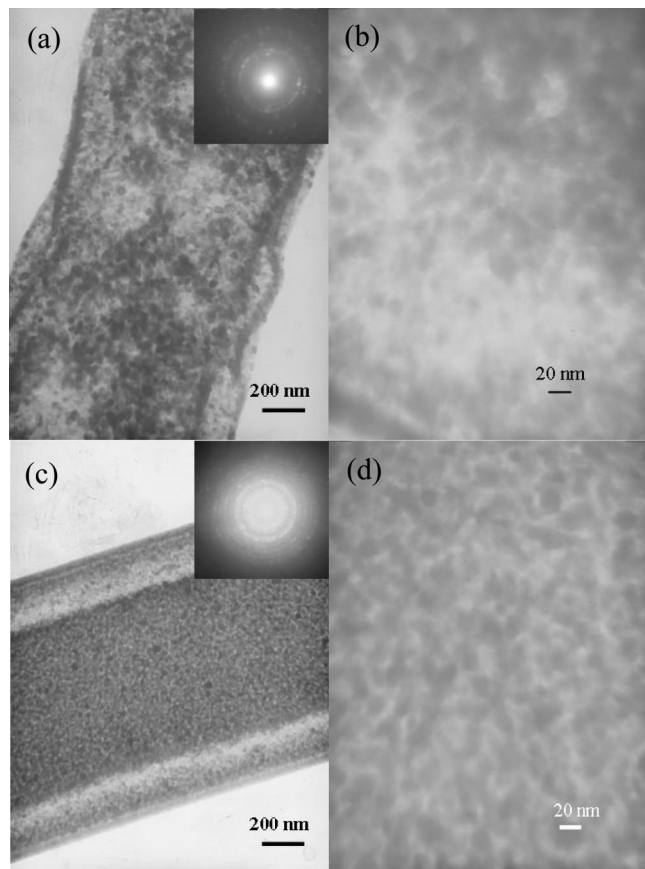
Preparation of Ferrite MFe$_2$O$_4$ Ribbons

J. Phys. Chem. B, Vol. 112, No. 36, 2008 **11295**

Figure 5. TEM images of the prepared ferrite ribbons calcined at 550 °C in air: (a) and (b) CoFe$_2$O$_4$ ribbons; (c) and (d) NiFe$_2$O$_4$ ribbons.
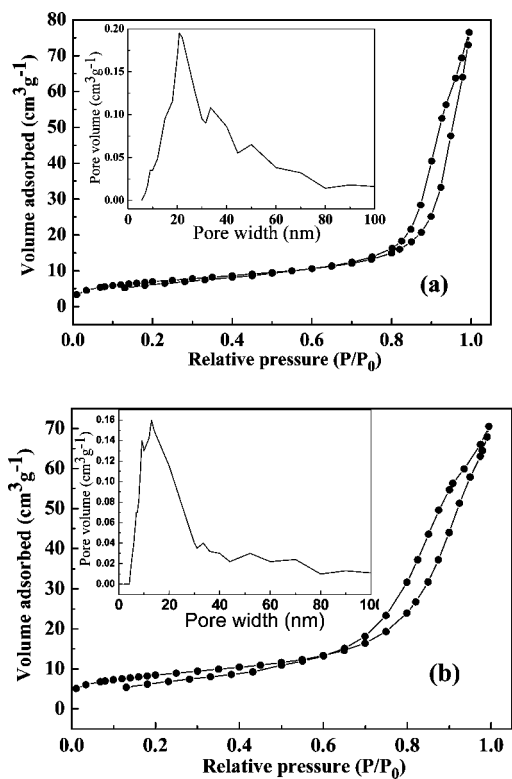

Figure 6. N$_2$ adsorption and desorption isotherms for CoFe$_2$O$_4$ (a) and NiFe$_2$O$_4$ (b) ribbons. The inset shows the BHJ pore size distributions of the ribbons.

thickness decreased to 400 nm. The size reduction was due to the loss of PVP from the precursor ribbons and the crystalliza-
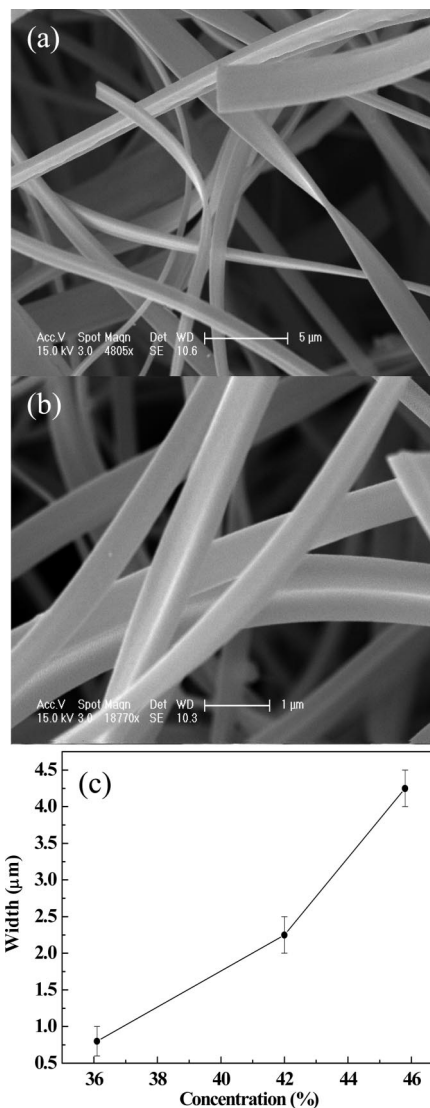

Figure 7. NiFe$_2$O$_4$ ribbons obtained at the precursor concentration of 42.0% (a) and 36.1% (b). (c) Concentration of precursor-width of the ribbon curve.

tion of the oxides. Figure 4b and d is an enlarged SEM image of CoFe$_2$O$_4$ and NiFe$_2$O$_4$ ribbons, from which relatively smooth surfaces of the ribbons are observed.

The microstructures of the ribbons were further investigated by transmission electron microscopy (TEM). Figure 5 shows TEM images of CoFe$_2$O$_4$ and NiFe$_2$O$_4$ ribbons after calcination, indicating that the ribbons were formed through the agglomeration of CoFe$_2$O$_4$ and NiFe$_2$O$_4$ nanoparticles with a domain size of 15−20 nm. The surface of the CoFe$_2$O$_4$ ribbons is not as flat as that of the NiFe$_2$O$_4$ ribbons. The selected area electron diffraction patterns (inset of Figure 4a and c) of the CoFe$_2$O$_4$ and NiFe$_2$O$_4$ ribbons show polycrystalline rings and are both indexed for cubic spinel structures. As observed, the surfaces of the ribbons have a lot of pores between particles (Figure 4b and d are the enlarged images). During the decomposition of PVP and inorganic salts, much gas was released and led to the porous structures between nanoparticles.

Figure 6a and b show N$_2$ adsorption/desorption isotherms for CoFe$_2$O$_4$ and NiFe$_2$O$_4$ ribbons, which were treated at 120 °C for 2 h under vacuum before testing. Both isotherms can be identified as type IV, which is characteristic of mesoporous materials. The pore size distribution of CoFe$_2$O$_4$ and NiFe$_2$O$_4$ ribbons is shown in the inset of Figure 6a and b. The peak is
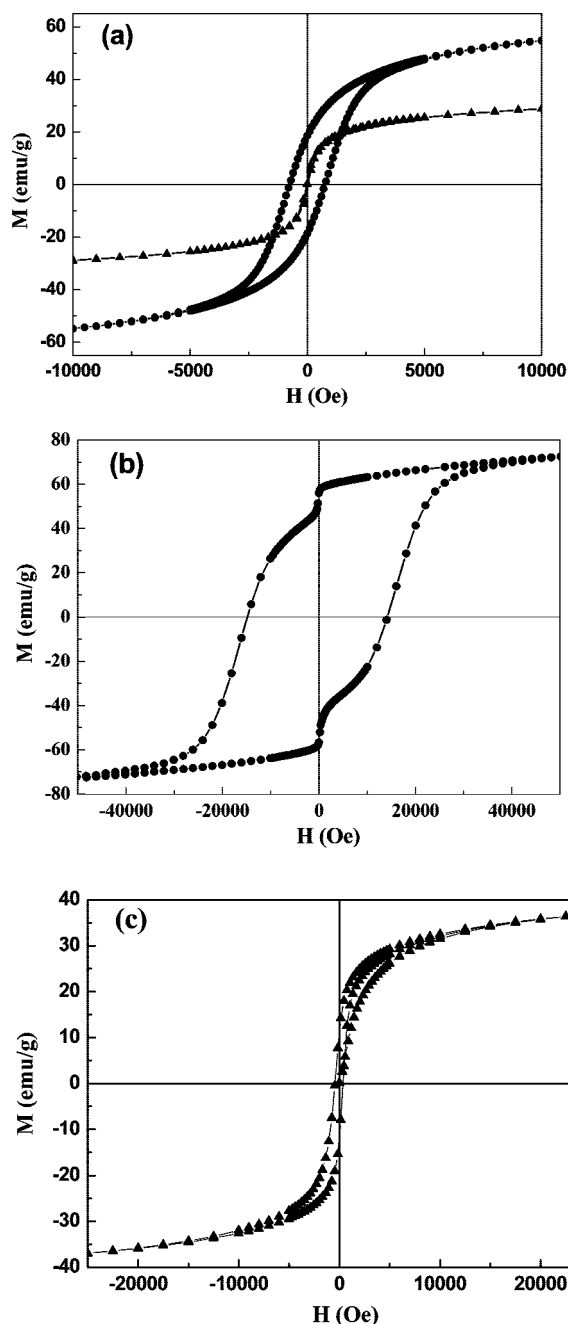
Figure 8. Magnetic properties of the electrospun $CoFe_2O_4$ (●) and $NiFe_2O_4$ (▲) ribbons: (a) at room temperature (300 K); (b) and (c) at low temperature (2 K).

TABLE 2: Magnetic Properties of Synthesized $CoFe_2O_4$ and $NiFe_2O_4$ Ribbons

	$CoFe_2O_4$ ribbons		$NiFe_2O_4$ ribbons	
	300 K	2 k	300 K	2 K
M_s (emu/g)	56	72	29	37
M_r (emu/g)	18	56	1	12
H_c (Oe)	757	14507	21	400

centered around 20 nm for $CoFe_2O_4$ ribbons and 15 nm for $NiFe_2O_4$ ribbons, which are in good agreement with the values evaluated from the TEM images. The generation of porosity is due to the interspace between nanoparticles; therefore, the pore size distribution is very broad. Some pores are larger than 50 nm. The Brunauer–Emmett–Teller (BET) surface areas of porous $CoFe_2O_4$ and $NiFe_2O_4$ ribbons are 23.7 and 28.8 m^2 g^{-1}, respectively.

3.3. Effect of the Concentration of the Precursor. Up to now, most of the electrospun products reported have been fibers or nanofibers, but ribbons could be obtained by controlling the spinning conditions. Li and co-workers have reported that by increasing the concentration of the sol–gel precursor and feeding rate while electrospinning in a low-humidity environment, flat ribbons with a mesoporous structure could be fabricated.[21] Here, the effect of the concentration of precursor was investigated. In order to demonstrate the relationship between the width of the ribbons and the concentration of the precursor, we carried out a series of experiments (Table 1) by keeping the ratio of inorganic salts to PVP at 0.5 and gradually decreasing the total amount of PVP and inorganic salts in the same solvent. The $NiFe_2O_4$ ribbons in Figure 4c and 7a and b were obtained at precursor concentrations of 45.8%, 42.0%, and 36.1%, respectively. As observed, the width of the ribbons reduced with decreasing concentration of the precursor (Figure 7c). The concentration of the precursor affected the splitting degree of the charged jet during the electrospinning process. High concentration led to incomplete splitting. From the cross section of the precursors (inset of Figure 1a and b), it can be observed that the ribbons seem to be made up of two parallel fibers. Interestingly, when the concentration of precursor decreased from 45.8% to 36.1%, the ribbon-like structure remained. As Li and co-workers have reported, the formation of the ribbon-like structure refers to many factors such as the properties of electrospinning solution, various electrospinning parameters, etc.[21] A detailed study is underway.

3.4. Magnetic Characterization. Magnetic properties were measured by a superconducting quantum interference device. Figure 8 shows the hysteresis loops of $CoFe_2O_4$ and $NiFe_2O_4$ ribbons at room temperature (300 K) and low temperature (2 K). The saturation magnetization (M_s), remanent magnetization (M_r), and coercivity (H_c) are summarized in Table 2. The magnetic properties of the magnetic materials have been believed to be dependent on the sample shape, crystallinity, magnetization direction, etc. In this experiment, the ribbons were formed through the agglomeration of magnetic nanoparticles, but their sizes were close to bulk values; therefore, their magnetic properties should be between nanoparticles and bulks. At 300 K, the saturation magnetization values of $CoFe_2O_4$ and $NiFe_2O_4$ ribbons are 56 and 29 emu/g, respectively, which are smaller than bulk values of 80.8[26] and 47.5[4] emu/g but higher than the nanoparticles reported.[27,28] The agglomeration of magnetic nanoparticles increased interaction between them. The reduction of M_s relatively to bulk is mainly due to the decreased particle size and spin canting at the surface of ferrite nanoparticles.[29] The coercivity of $CoFe_2O_4$ ribbons was 757 Oe, and $NiFe_2O_4$ ribbons exhibited superparamagnetism at 300 K. From the reported results, it can be seen that magnetic properties are also influenced by the synthesis process. The influence of our preparation method on magnetic properties is under study.

At low temperature, the M_s increased to 72 emu/g for $CoFe_2O_4$ ribbons and 37 emu/g for $NiFe_2O_4$ ribbons, which is close to the theoretical values. The coercivities increase a lot as temperature goes down, especially for $CoFe_2O_4$. At 2 K, the coercivities for $CoFe_2O_4$ and $NiFe_2O_4$ ribbons are 1.45 T and 400 Oe, respectively. Changes of magnetic properties could be attributed to noncollinear spin structure originating from the pinning of the surface spins, which were explained by the core–shell model of nanoparticles.[30,31] The core is constituted of moments magnetically coupled, and the surface is formed of disordered moments. The existence of a spin-glass shell in ferrite nanoparticles can be rationalized by the broken exchange

Preparation of Ferrite MFe$_2$O$_4$ Ribbons

J. Phys. Chem. B, Vol. 112, No. 36, 2008 **11297**

bonds at its surface. At the surface of the grains, the variations in coordination of cations and bond breaking may result in a distribution of exchange fields as well as spin canting or perturbations in crystal field inducing surface anisotropy.[32] When the applied fields are high enough at low temperature, the surface anisotropy is overcome, and the surface spins tend to align the field direction, which results in a higher M_s value. The dramatic increase in coercivities at low temperature originates from exchange anisotropy due to spin disorder at the particle surface. This effect is expected to be larger for smaller particles when the surface to volume ratio increases. Interestingly, the hysteresis loop of CoFe$_2$O$_4$ ribbons at low temperature exhibits a constricted phenomenon. There are two possible reasons for this phenomenon: (1) the sizes of nanocrystals within the ribbons are not uniform, and nanocrystals with sizes smaller than 10 nm exist (Figure S1, Supporting Information); (2) ribbon-like microstructures have influence with the low temperature magnetic properties. In order to investigate this phenomenon, two groups of comparison are done (Figure S2, Supporting Information). It is clearly seen that this phenomenon weakens much when CoFe$_2$O$_4$ ribbons are calcined at 550 °C for 6 h. More interestingly, although the sizes of particles within nanoribbons and microribbons are similar, the hysteresis loop of nanoribbons does not exhibit the constricted phenomenon at all (Figure S2b, Supporting Information).

4. Conclusions

In summary, MFe$_2$O$_4$ (M = Co, Ni) ribbons with nanoporous structure were prepared by electrospinning combined with simple sol−gel technology. The ribbons formed through the agglomeration of magnetic nanoparticles with PVP as the structure directing template. The effect of sol−gel precursor concentration was investigated. Porous structure was formed during the decomposition of PVP and inorganic salts. The ribbons exhibited weak saturation magnetizations and low coercivities at room temperature, but at low temperature saturation magnetizations and coercivities increased a lot. These novel magnetic ribbons can potentially be used in micro/nano electronic devices, gas sensors, and catalysts.

Supporting Information Available: TEM images of CoFe$_2$O$_4$ ribbons calcined at 550 °C for 2 and 6 h; comparison of low temperature magnetic properties CoFe$_2$O$_4$ ribbons calcined at 550 °C for 2 h and 6 h; comparison of low temperature magnetic properties between CoFe$_2$O$_4$ nanoribbons 600 °C for 1 h and microribbons 550 °C for 2 h; and TEM image of CoFe$_2$O$_4$ nanoribbons calcined at 600 °C for 1 h. This material is available free of charge via the Internet at http://pubs.acs.org.

References and Notes

(1) Sugimoto, M. *J. Am. Ceram. Soc.* **1999**, *82*, 269.
(2) Yu, S. H.; Yoshimura, M. *Chem. Mater.* **2000**, *12*, 3805.
(3) Xuan, S. H.; Hao, L. Y.; Jiang, W. Q.; Song, L.; Hu, Y.; Chen, Z. Y.; Fei, L. F.; Li, T. W. *Cryst. Growth Des.* **2007**, *7*, 430.
(4) Bao, N.; Shen, L.; Wang, Y.; Padhan, P.; Gupta, A. *J. Am. Chem. Soc.* **2007**, *129*, 12374.
(5) Mooney, K. E.; Nelson, J. A.; Wagner, M. J. *Chem. Mater.* **2004**, *16*, 3155.
(6) Liu, C.; Zou, B.; Rondinone, A. J.; Zhang, Z. J. *J. Am. Chem. Soc.* **2000**, *122*, 6263.
(7) Zhang, Z. J.; Wang, Z. L.; Chakoumakos, B. C.; Yin, J. S. *J. Am. Chem. Soc.* **1998**, *120*, 1800.
(8) Ji, G.; Tang, S.; Xu, B.; Gu, B.; Du, Y. *Chem. Phys. Lett.* **2003**, *379*, 484.
(9) Keller, N.; Pham-Huu, C.; Estournes, C.; Greneche, J. M.; Ehret, G.; Ledoux, M. J. *Carbon* **2004**, *42*, 1395.
(10) Pham-Huu, C.; Keller, N.; Estournès, C.; Ehret, G.; Ledoux, M. J. *Chem. Commun.* **2002**, 1882.
(11) Kinsella, J. M.; Ivanisevic, A. *J. Phys. Chem. C* **2008**, *112*, 3191.
(12) Altavilla, C.; Ciliberto, E.; Aiello, A.; Sangregorio, C.; Gatteschi, D. *Chem. Mater.* **2007**, *19*, 5980–5985.
(13) Lee, D. K.; Kim, Y. H.; Kang, Y. S.; Stroeve, P. *J. Phys. Chem. B* **2005**, *109*, 14939–14944.
(14) Li, D.; Wang, Y.; Xia, Y. *Adv. Mater.* **2004**, *16*, 361.
(15) Wu, H.; Zhang, R.; Liu, X.; Lin, D.; Pan, W. *Chem. Mater.* **2007**, *19*, 3506.
(16) Li, D.; Herricks, T.; Xia, Y. *Appl. Phys. Lett.* **2003**, *83*, 4586.
(17) Li, D.; Wang, Y.; Xia, Y. *Nano. Lett.* **2003**, *3*, 1167.
(18) Yang, X. H.; Shao, C. L.; Guan, H. Y.; Li, X. L.; Gong, H. *Inorg. Chem. Commun.* **2004**, *7*, 176.
(19) Wang, G.; Ji, Y.; Huang, X.; Yang, X.; Gouma, P. I.; Dudley, M. *J. Phys. Chem. B* **2006**, *110*, 23777.
(20) Zhan, S.; Chen, D.; Jiao, X.; Tao, C. *J. Phys. Chem. B* **2006**, *110*, 11199.
(21) Li, D.; McCann, J. T.; Xia, Y. *J. Am. Ceram. Soc.* **2006**, *89*, 1861.
(22) Larsen, G.; Noriega, S.; Spretz, R.; Velarde-Ortiz, R. *J. Mater. Chem.* **2004**, *14*, 2372.
(23) Zhang, Y.; Li, J.; Li, Q.; Zhu, L.; Liu, X.; Zhong, X.; Meng, J.; Cao, X. *Scr. Mater.* **2007**, *56*, 409.
(24) Azhari, S. J.; Diab, M. A. *Polym. Degrad. Stab.* **1998**, *60*, 253.
(25) Vestal, C. R.; Song, Q.; Zhang, Z. J. *J. Phys. Chem. B* **2004**, *108*, 18222.
(26) Grigorova, M.; Blythe, H. J.; Rusanov, V.; Petkov, V.; Masheva, V.; Nihtianova, D.; Martinez, L. M.; Munoz, J. S.; Mikhov, M. *J. Magn. Magn. Mater.* **1998**, *183*, 163.
(27) Shafi, K. V. P. M.; Gedanken, A.; Prozorov, R.; Balogh, J. *Chem. Mater.* **1998**, *10*, 3445.
(28) Jiang, J.; Yang, Y. M.; Li, L. C. *Mater. Lett.* **2008**, *62*, 1973.
(29) Coey, J. M. D. *Phy. Rev. Lett.* **1971**, *27*, 1140.
(30) Haneda, K.; Morrish, A. H. *J. Appl. Phys.* **1988**, *63*, 4528.
(31) Kodama, R. H.; Berkowitz, A. E.; McNiff, E. J.; Foner, S. *Phy. Rev. Lett.* **1996**, *77*, 394.
(32) Manova, E.; Kunev, B.; Paneva, D.; Mitov, I.; Petrov, L.; Estournes, C.; DOrleans, C.; Rehspringer, J. L.; Kurmoo, M. *Chem. Mater.* **2004**, *16*, 5689.